



OPEN Highly sensitive cancer detection using an open D-channel PCF-based SPR biosensor

Mahla Ashrafi¹, Saeed Olyae^{1,2✉} & Mahmood Seifouri²

Surface plasmon resonance (SPR) is a technique utilized for the label-free detection of cancer cells. In this analysis, we introduce a photonic crystal fiber (PCF) designed with an open D-channel, featuring a layer of gold (Au) and titanium dioxide (TiO₂) as the plasmonic material. This effectively reduces the gap between the fiber core and the gold layer, resulting in improved performance. Additionally, incorporating TiO₂ between the gold and the silica substrate enhances their adhesion and contributes to a more robust structure. We conducted a comprehensive numerical analysis of the suggested biosensor utilizing the finite element method (FEM) integrated with perfectly matched layers (PML) within the COMSOL Multiphysics simulation tool. The design of this sensor is specifically intended for the detection of molecules with a refractive index (RI) varying from 1.25 to 1.43, achieving an impressive peak spectral sensitivity of 47,000 nm/RIU. For this purpose, we investigated RI values from 1.36 to 1.401 concerning six different cancer cell types. The highest spectral sensitivity is 5214.285 nm/RIU, while the amplitude sensitivity is -1481.1 RIU⁻¹, which has been recorded for MCF-7 and HeLa cells. This proposed sensor shows improved amplitude sensitivity, signal-to-noise ratio (SNR), full width at half maximum (FWHM), figure of merit (FOM), and detection limit (DL) compared to existing biosensors, highlighting its potential for biosensing applications. Additionally, it is significant that according to the results, HeLa cells have a maximum resolution of 1.19×10^{-5} RIU and a FOM of 350 RIU⁻¹.

Keywords Photonic crystal fiber (PCF), Biosensor, Surface plasmon resonance (SPR), Microchannel, Cancerous cells

In recent decades, cancer research has gained significant attention due to the disease's severity and treatment challenges. Cancer occurs when healthy cells undergo changes that lead to the formation of cancerous cells. Biosensors enable quick cancer diagnosis by detecting specific chemicals in biological samples. They identify molecules like antibodies or enzymes, allowing for early detection of cancer cells, which is crucial for improving treatment outcomes^{1–3}. Biosensors are categorized into three primary types based on their bio-transducer; Acoustic, Optical, and Thermal biosensors. In 1962, Clark and Lyons pioneered the optical sensing system, leading to various applications for optical sensors. Sensors convert biological data into optical signals by tracking light property changes when interacting with substances. Many optical sensors depend on spectral features, such as a distinct peak or slope, arising from resonance. Variations in the refractive index (RI) lead to intensity or wavelength shifts, which are used to monitor changes in the analyte's RI^{4,5}.

Optical biosensors can be classified on two criteria; Label and Label-free. Detection usually requires labels like enzymes or fluorescent markers that bind to the target analyte. The measurement signal depends on the amounts of target analytes and labels. Various labeling techniques include electrochemically active probes, chemiluminescence, and fluorescent labeling. However, this process can be costly, time-consuming, and may interfere with receptor-analyte interactions⁶. An alternative diagnostic method that is highly recommended is label-free detection. This technique eliminates labels and encompasses methods such as localized surface plasmon resonance (LSPR), mass spectrometry, microcantilevers, and surface plasmon resonance (SPR). These techniques detect analytes based on intrinsic physical characteristics like charge, dielectric constant, refractive index changes, and size. Sensors that use SPR allow for quick and accurate detection of various analytes, are resistant to electromagnetic interference, and are ideal for remote monitoring and real-time analysis^{6–8}. SPR-based biosensors and photonic crystal fibers (PCFs) are being explored due to their unique cladding region,

¹Nano-Photonics and Optoelectronics Research Laboratory (NORLab), Shahid Rajaee Teacher Training University, Tehran 16788-15811, Iran. ²Faculty of Electrical Engineering, Shahid Rajaee Teacher Training University, Tehran, Iran. ✉email: s_olyae@sru.ac.ir

which features numerous small holes that manipulate light propagation in the core. PCFs utilize photonic band gap and total internal reflection (TIR) principles, making them robust, compact, and cost-effective. By adjusting the size and arrangement of these holes, a variety of designs can be created to meet specific needs⁹.

Biosensors can be categorized by fiber geometry into circular, D-shaped, slotted, and bowl-shaped designs. Also, incorporating microchannels in D-shaped structures can enhance performance. These sensors detect gases and a variety of analytes, including cancer, DNA, glucose, blood components, proteins, and malaria^{10–14}. The traditional techniques for cancer diagnostics consist of magnetic resonance imaging, ultrasound, positron emission tomography (PET scans), or mammography¹⁵. Currently, surface plasmon sensors are preferred over traditional optical biosensor techniques due to their superior sensitivity. They also offer additional benefits, such as ease of use and the ability to operate without requiring expert knowledge. Furthermore, surface plasmon sensors are capable of detecting cancer in its early stages, with an average cost of approximately USD ~6,000¹⁶. In contrast, the colorimetric method is a more affordable option, averaging around USD ~800. However, this method is prone to significant errors, necessitates expert handling, and is only effective for detecting cancer in its later stages¹⁷. Similarly, optical coherence tomography requires a specialist for late-stage cancer diagnosis and has the highest average cost, around USD ~7,164¹⁸. Plasmonic materials in PCF-based SPR biosensors can be used internally and externally. Internally structured sensors offer high sensitivity due to direct light-analyte interaction, but challenges include achieving uniform plasmonic coatings in small air holes and usability issues from liquid penetration. Externally structured PCF sensors, on the other hand, detect analytes at the surface, where ligands bind to sample molecules. This results in changes in RI, which correlate linearly with wavelength, producing a Gaussian-shaped confinement loss curve for sensitivity assessment in both wavelength and amplitude measurements^{15,19,20}.

In 2020 Anik et al.²¹ reported a milled microchannel and open D-channel PCF SPR biosensor placed at the bottom and top, using Au/TiO₂ as a plasmonic layer. Above the microchannel and below the D-channel, air holes with diameters $da_1 = 1.27 \mu\text{m}$ and $da_2 = 1.20 \mu\text{m}$ are positioned to create a stable core mode. Also, we can see $da_3 = 1.65 \mu\text{m}$ and $da_4 = 2.2 \mu\text{m}$ in the inner and outer rows of a square lattice. The best thickness of 80 nm and 9 nm is found for gold and TiO₂ respectively. The height of the U-shaped groove and D-channel radius are 4.83 μm and 2.40 μm . The detection range is between 1.14 and 1.36, with a peak sensitivity of 53,800 nm/RIU.

In 2023, Yang et al.²² developed a biosensor using photonic crystal fiber with double gold nanowires ($d_3 = 0.8 \mu\text{m}$ diameter) and a circular lattice design featuring holes of $d_1 = 1.8 \mu\text{m}$ diameter. Small air holes ($d_2 = 1.4 \mu\text{m}$) near the nanowires help leak core energy to the plasmonic material. This design shows promising results for MCF-7 cells, featuring a spectral sensitivity of 16,357 nm/RIU and amplitude sensitivity (AS) of $-1,242 \text{ RIU}^{-1}$.

This year, Abdelghaffar et al.²³ reported a V-shaped photonic crystal biosensor that utilizes plasmonic materials for the early detection of cervical, basal, and breast cancer cells. This biosensor features a hexagonal lattice with air holes that have a radius of 2.35 μm , spaced at a distance of 6.73 μm . The plasmonic material used is zirconium nitride (ZrN) with a thickness of 30 nm. The structure demonstrates impressive sensitivity in the TM mode, with values of 5,008.33, 3,800, and 6,214.28 nm/RIU, and in the TE mode, with values of 5,333.3, 4,400, and 6,000 nm/RIU.

Also, Ibrahim et al.²⁴ introduced a twin-core PCF SPR biosensor that utilizes a TiO₂/Au with thicknesses of $t_t = 12 \text{ nm}$ and $t_g = 25 \text{ nm}$ as the plasmonic layer. Additionally, the geometric parameters were established as $t_a = 1.3 \mu\text{m}$, $p = 1.8 \mu\text{m}$, $d_1 = 380 \text{ nm}$, $d_2 = 0.75 \mu\text{m}$, and $d_3 = 1.5 \mu\text{m}$. This biosensor exhibits a strong response to six varieties of cancerous cells, demonstrating a sensitivity of 4,078.43 nm/RIU, an amplitude sensitivity of $-4,285.71 \text{ RIU}^{-1}$, and a resolution of $4 \times 10^{-5} \text{ RIU}$ for HeLa, MCF-7, and basal cells, respectively.

Our proposed D-shaped SPR-based PCF biosensor features a microchannel along its flat side, which improves performance and aids in light coupling by positioning the analyte nearer to the core. Gold (Au) coating is applied to the microchannel part of this device, while titanium dioxide (TiO₂) is utilized beneath it. Unlike methods that involve coating the entire fiber with plasmonic materials, this approach minimizes both the coating area and the complexity of polishing, resulting in lower costs. We have extensively optimized and analyzed the structural parameters, such as the hole diameters, the radius of the microchannel, the pitch, and the thicknesses of the Au and TiO₂ layers.

SPR-based PCF biosensor compositions

Design geometry of the suggested biosensor

The suggested biosensor underwent a detailed analysis employing the finite element method (FEM) with perfectly matched layers (PML) via COMSOL Multiphysics 6.2 software, ensuring precision and reliability in its performance evaluation. This design focuses on reducing the distance between the center of the structure and the plasmonic material, facilitating efficient signal and energy transfer from the core to the designated microchannel. This transition enhances the oscillation of electrons in the gold and TiO₂ region, generating a surface plasmon wave (SPW). Surface plasmon polarization occurs when the frequency of light incident from the core matches the frequency of the oscillating electrons. When this happens, at a specific wavelength and desired refractive index, the core-guided mode aligns with the surface plasmon polariton (SPP) mode, allowing maximum energy to be transferred to the free electrons⁸.

This structure utilizes three distinct hole sizes designated as d_1 , d_2 , and d_3 , with their effects and performance discussed later. The thickness of the Au and TiO₂ layers is denoted by t_{au} and t_r . Additionally, the radius of the open channel located at the top of the structure will be referred to as r . The pitch, or Λ , is the space between the center of two adjacent holes in a square lattice, denoted as P in this study. The sensor structure has undergone multiple simulations to optimize various parameters, during which the remaining parameters were held constant. After optimization, the parameter values are $P = 3.6 \mu\text{m}$, $r = 2.75 \mu\text{m}$, $d_1 = 1.75 \mu\text{m}$, $d_2 = 3.2 \mu\text{m}$, $d_3 = 1.3 \mu\text{m}$,

$t_{\text{au}} = 40 \text{ nm}$ and $t_t = 10 \text{ nm}$. To create the D-shaped design, the PCF fiber is polished from a distance of $h = 1.5 \times P \mu\text{m}$ from the core.

Figure 1a shows a cross-sectional view of the open D-channel biosensor. It reveals that the structure consists of three main parts. The first part is silica, which forms the internal component and features 16 circular air holes arranged in a square lattice. The two other sections of the proposed biosensor include a metallic plasmonic layer and an analyte channel. Commonly used plasmonic materials in biosensors include gold, silver, aluminum, and copper. To enhance sensor performance, materials such as graphene, zinc oxide, and MoS_2 are also employed, with Au being preferred due to its chemical stability^{19,25}. Additionally, gold offers advantages over silver and other plasmonic materials due to its notable variations in resonance wavelengths. Silver, for example, is highly susceptible to rapid oxidation, which reduces its sensitivity and creates challenges for long-term use. In contrast, gold demonstrates greater stability and biocompatibility, along with a wider plasmon resonance bandwidth. These attributes make gold more suitable for biosensor applications, as it allows for greater flexibility in design and optimization^{24,26}. While gold is not completely immune to oxidation, it surpasses the previously mentioned plasmonic materials, and several strategies have been suggested to reduce the impact of oxidation on sensor performance. These strategies include utilizing high-quality gold, applying protective coatings, employing appropriate storage techniques, and minimizing exposure to oxygen or water²⁷. Therefore, the gold layer is integrated into the microchannel section of this structure. A thin layer of titanium dioxide bonds Au to silica, enhancing plasmon-analyte interaction and solving positioning and fabrication challenges. Placing the microchannel within the D-shaped section of the biosensor minimizes the amount of plasmonic material needed, streamlining the manufacturing process and improving performance. The outer part of the proposed structure features an analyte channel and a PML layer, measuring $3.5 \times P \mu\text{m}$ and $0.8 \times P \mu\text{m}$ in thickness, respectively. The PML is designed to mitigate undesired non-physical emissions at the surface. This sensor is designed using the commonly employed stack and draw method. Figure 1b illustrates a 2D stacking diagram of the sensor, which includes solid, thin-walled, and thick-walled capillaries.

Figure 2 presents a schematic representation of the suggested biosensor that employs surface plasmon resonance. This configuration indicates that the optical fiber connects to a broadband source (BBS), enabling the photonic crystal fiber to receive broad-spectrum light. The SPR effect arises from light transmission through the fiber and alterations in the refractive index near the sensor's surface, which makes the sensor extremely responsive to changes. The fiber connects to an optical spectrum analyzer (OSA) and a laptop for data collection, allowing real-time monitoring of the interference spectrum. The biosensor features a chamber designed for the introduction and extraction of liquid tissue samples suspected of containing cancerous cells. Additionally, a pressure pump is utilized to circulate the fluid through the system. After each testing session, deionized water can be used to clean the area, thereby preparing the sensor for subsequent tests with new samples. The samples being analyzed are obtained through liquid biopsy from tumors^{13,28,29}.

Conceptual analysis

The proposed biosensor is constructed using materials such as Au, TiO_2 , and fused silica. Silica has been selected as the substrate material because of its outstanding mechanical durability and minimal absorption loss. The Sellmeier equation describes how the refractive index of silica changes with wavelength, denoted by n^{30} ,

$$n^2(\lambda) = \frac{B_1\lambda^2}{\lambda^2 - C_1} + \frac{B_2\lambda^2}{\lambda^2 - C_2} + \frac{B_3\lambda^2}{\lambda^2 - C_3} \quad (1)$$

The Sellmeier constants are defined as $B_1 = 0.69616300$, $B_2 = 0.407942600$, $B_3 = 0.897479400$, $C_1 = 0.00467914826$, $C_2 = 0.0135120631$, $C_3 = 97.9340025$, with λ denoting the wavelength.

The first plasmonic material defined is gold, and one method to coat microchannels with plasmonic materials is by using the chemical vapor deposition (CVD) process³¹. The dependence of dielectric constants on wavelength is known from the Drude-Lorentz model³²:

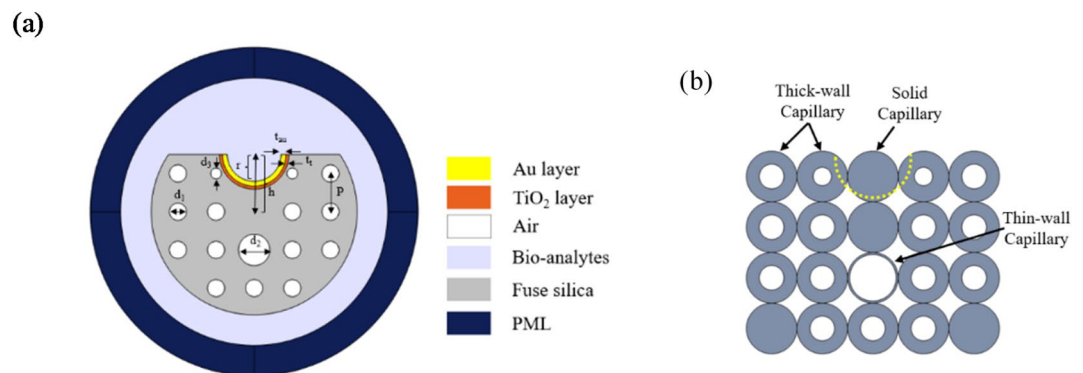


Fig. 1. Cross-sectional view of (a) proposed microchannel-based D-shaped biosensor, and (b) the stacked structure of the proposed PCF with solid, thick-walled, and thin-walled capillaries.

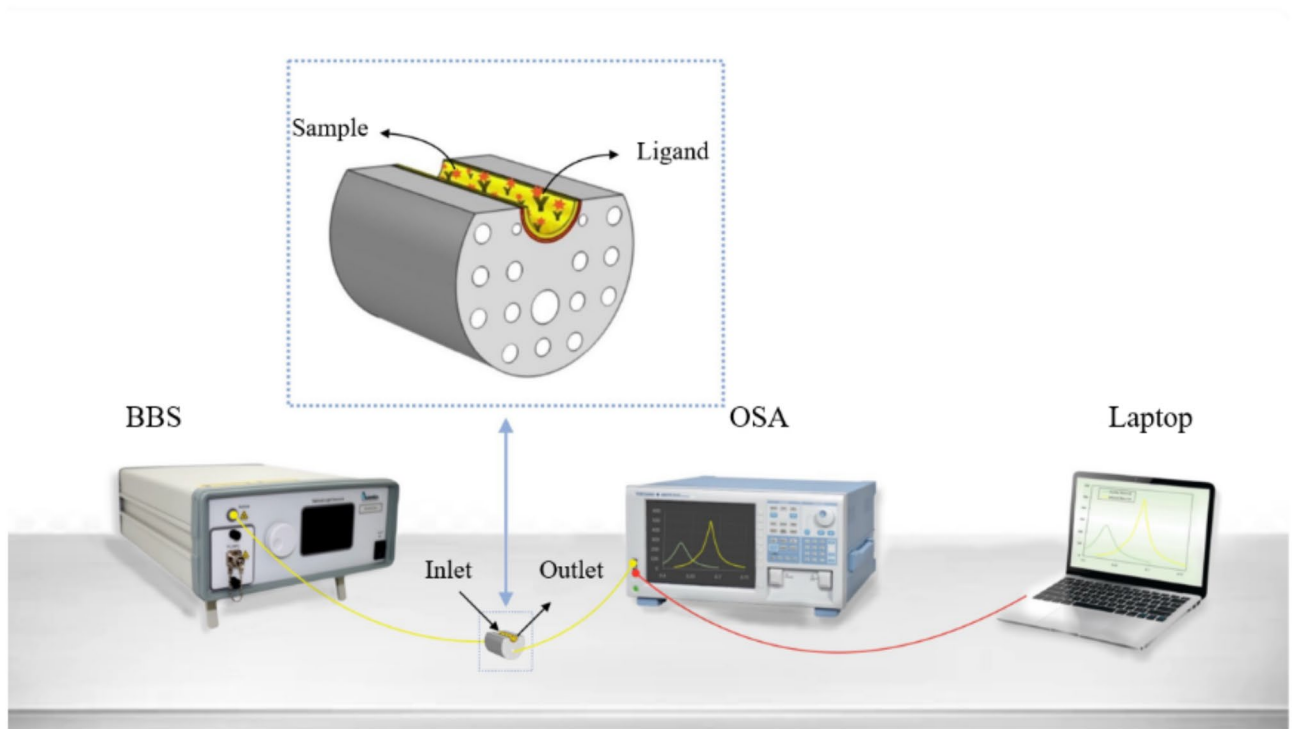


Fig. 2. Schematic of the proposed microchannel-based D-shaped sensor setup featuring a broadband source, optical spectrum analyzer, and a laptop for analyte detection.

$$\varepsilon_{Au} = \varepsilon_{\infty} - \frac{\omega_D^2}{\omega(\omega + j\gamma_D)} - \frac{\Delta\varepsilon\Omega_L^2}{(\omega^2 - \Omega_L^2) - j\Gamma_L\omega} \quad (2)$$

where ε_{Au} is the permittivity of gold, $\varepsilon_{\infty} = 5.9673$ is its permittivity at elevated frequencies. Additionally, $\omega = 2\pi c/\lambda$ represents the angular frequency where c is the speed of light in a vacuum. The plasma frequency is indicated by $\omega_D = 4,227.2\pi$ THz, while the damping frequency is represented by $\gamma_D = 31.84\pi$ THz. We also have a weighting factor denoted by $\Delta\varepsilon = 1.09$. Furthermore, $\Gamma_L = 209.72\pi$ THz represents the spectral width of the Lorentz oscillator and, $\Omega_L = 1,300.14\pi$ THz indicates the oscillator's strength.

The function $\varepsilon_{Au}(\omega)$ is expressed as $\varepsilon_{Au}(\omega) = \varepsilon_1(\omega) + j\varepsilon_2(\omega)$, linking to angular frequency. The complex refractive index of the medium, $\tilde{n}(\omega) = n(\omega) + jk(\omega)$, represents the square root of ε . This, along with reflectivity studies at optical frequencies, aids in measuring ε .

$$\varepsilon_{Au} = \varepsilon_1 + j\varepsilon_2 \quad (3)$$

$$\varepsilon_1 = \text{Re}(\varepsilon_{Au}) \quad (4)$$

$$\varepsilon_2 = \text{Im}(\varepsilon_{Au}) \quad (5)$$

$$\varepsilon_1 = n_{Au}^2 - k^2 \quad (6)$$

$$\varepsilon_2 = 2n_{Au}k \quad (7)$$

$$n_{Au} = \sqrt{\frac{\varepsilon_1}{2} + \frac{1}{2}\sqrt{(\varepsilon_1^2 + \varepsilon_2^2)}} \quad (8)$$

$$k_{Au} = \frac{\varepsilon_2}{2n_{Au}} \quad (9)$$

The extinction coefficient, denoted as k , defines the extent of optical absorption experienced by electromagnetic waves as they interact with various materials³³.

TiO₂ is selected due to its elevated refractive index compared to the fiber, which improves the interaction between the core and the plasmonic mode. It also efficiently absorbs the field from the core mode. Furthermore, this material is safe for the environment and non-toxic³⁴. The RI profile of TiO₂ can be evaluated from³⁵:

$$n_{\text{TiO}_2}(\lambda) = \sqrt{5.913 + \frac{2.441 \times 10^7}{\lambda^2 - 0.803 \times 10^7}} \quad (10)$$

where n_{TiO_2} denotes the refractive index of TiO_2 .

To assess the sensing capability, confinement loss (CL) serves as an important introductory factor, which can be articulated using³⁶:

$$\alpha \left[\frac{\text{dB}}{\text{cm}} \right] = 8.686 \times k_0 \times \text{Im} [n_{\text{eff}}] \times 10^4 \quad (11)$$

$k_0 = 2\pi/\lambda$ represents the wave vector in free space, while $\text{Im} [n_{\text{eff}}]$ denotes the imaginary component of the effective refractive index.

Spectral sensitivity, also referred to as wavelength sensitivity (WS), is a crucial factor in assessing how effective PCF-SPR biosensors are, which can be determined by²²:

$$S_\lambda \left[\frac{\text{nm}}{\text{RIU}} \right] = \frac{\Delta \lambda_{\text{peak}}}{\Delta n_a} \quad (12)$$

In cancer cells, $\Delta \lambda_{\text{peak}}$ and Δn_a represent the differences in wavelengths associated with the peak loss and the changes in the refractive index between healthy and affected cells for each type of cancer.

An additional key technique is the amplitude interrogation method, which is established by mapping the sensor power loss spectrum that corresponds to the refractive index of the analyte at a particular wavelength and can be defined as²⁹:

$$S_A(\lambda) [\text{RIU}^{-1}] = -\frac{1}{\alpha(\lambda, n_a)} \frac{\delta \alpha(\lambda, n_a)}{\delta n_a} \quad (13)$$

$\alpha(\lambda, n_a)$ represents the CL of the fundamental core mode at a specific wavelength, while $\delta \alpha(\lambda, n_a)$ signifies the variation between two adjacent spectral losses.

The resolution of the suggested biosensor is assessed by³⁷:

$$R [\text{RIU}] = \frac{\Delta n_a \times \Delta \lambda_{\text{min}}}{\Delta \lambda_{\text{peak}}} \quad (14)$$

where $\Delta \lambda_{\text{min}} = 0.1 \text{ nm}$ represents the minimum spectral resolution; $\Delta \lambda_{\text{peak}}$ signifies the change in the resonant wavelength, while Δn_a indicates the modification in the cells' refractive index.

One important parameter that enhances sensor performance is the figure of merit (FOM)^{12,38}:

$$\text{FOM} [\text{RIU}^{-1}] = \frac{S_\lambda}{\text{FWHM} (\text{nm})} \quad (15)$$

FWHM refers to the full width at half maximum and quantifies the width of the confinement loss peak. A narrower FWHM may lead to a decrease in spectral noise.

Signal-to-noise ratio (SNR) indicates the strength of the resonance peak compared to the background noise and can be evaluated from³⁸:

$$\text{SNR} [\text{dB}] = \frac{\Delta \lambda_{\text{peak}}}{\text{FWHM} (\text{nm})} \quad (16)$$

The minimum quantity of a biological item that can be detected by the sensor is referred to as the detection limit, which can be expressed in terms of FWHM and SNR³⁰:

$$\text{DL} [\text{nm}] = \frac{\text{FWHM} (\text{nm})}{1.5(\text{SNR})^{0.25}} \quad (17)$$

Feasibility of fabricating the proposed PCF biosensor

This section explores the feasibility of fabricating Photonic Crystal Fibers, with an emphasis on the practicality of producing a specific fiber structure. Given the numerous advantages of PCF over conventional fibers, various techniques are employed to manufacture the proposed sensor, including sol-gel processing, stack-and-draw methods, and die-casting³⁰. In Fig. 3, the fabrication steps for the microchannel-based D-shaped biosensor are illustrated. The stack and draw technique provides a scalable and adaptable method for fabricating photonic crystal fibers, enabling complex structures such as square, circular, and triangular lattices. The process of fabricating a PCF rod preform involves using distinct silica capillaries of varying thickness along with a solid silica rod. These capillaries and rods are organized and arranged based on the intended sensor lattice design. After the stacking process, the preform is drawn down to a rod scale, enabling careful regulation of the temperature and the drawing speed to create fibers with specific dimensions. Following the stacking, one section of the circular PCF can be etched to transform it into a D-shaped PCF^{30,39}. A microchannel can be created in the etched region using focused ion beam milling or femtosecond laser micromachining, with chemical etching also used to speed up the process in photonic crystal fiber^{40–42}. The design of the D-shaped photonic crystal fiber enables easy filling of the sensing area with analyte. During the fabrication process, careful consideration of layer deposition is crucial to avoid air bubbles and to maintain a consistent distribution of metallic layers. An uneven distribution can cause scattering, which can undermine the effective confinement of optical signals and

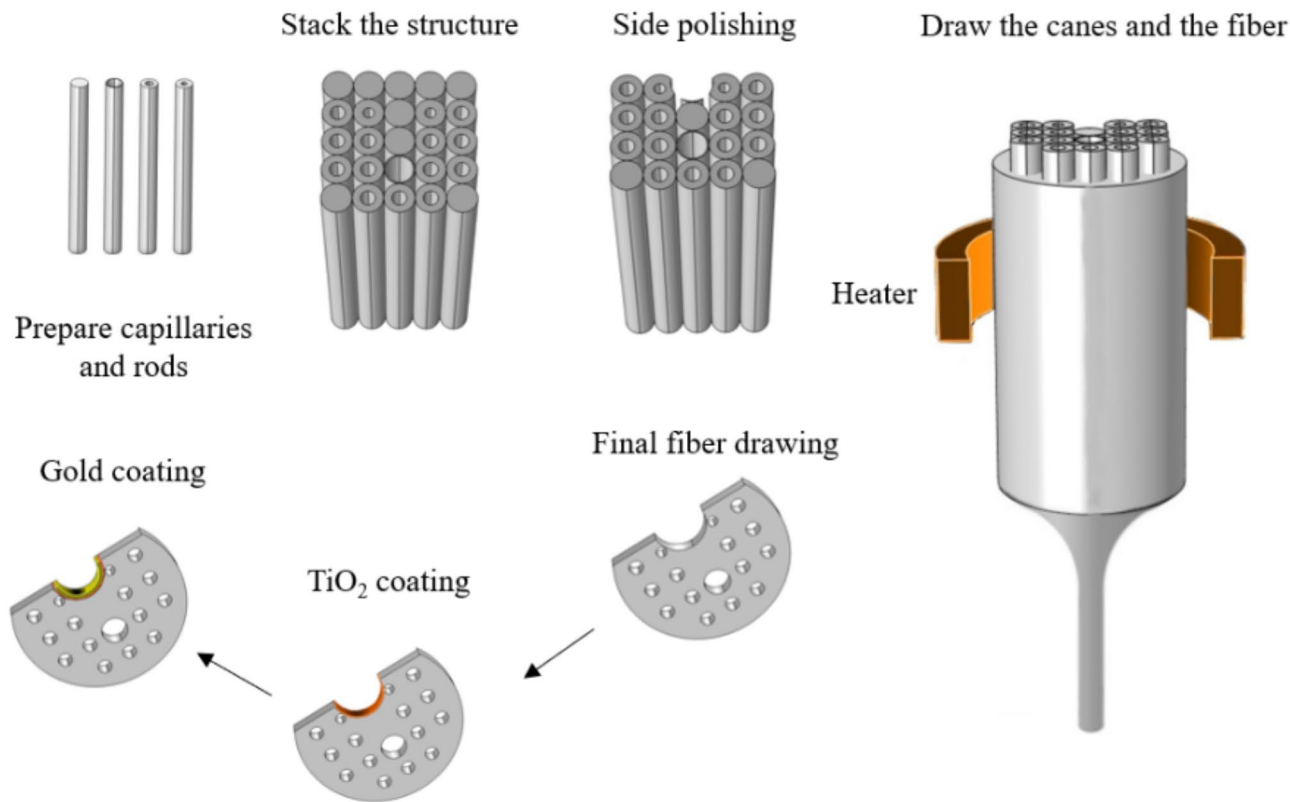


Fig. 3. Illustration of the possible fabrication scheme for the proposed biosensor.

Cancer	Associated cell	Refractive index		Change in refractive index
		Healthy cell	Cancerous cell	
Cervical	HeLa	1.368	1.392	0.024
Adrenal gland	PC12	1.381	1.395	0.014
Blood	Jurkat	1.376	1.390	0.014
Skin	Basal cell	1.360	1.380	0.020
Breast	MDA-MB-231	1.385	1.399	0.014
Breast	MCF-7	1.387	1.401	0.014

Table 1. The refractive index variation for normal cells and cancerous cells²².

may diminish sensor performance⁴³. According to recent reports, atomic layer deposition (ALD) is used to apply plasmonic materials to the microchannel Sect⁴⁴. Also, the chemical vapor deposition technique can be applied to surfaces with different geometries to produce high-quality, oriented thin films that resist solvent damage and offer consistent thicknesses of low-porosity coatings⁴⁵.

Result and numerical analysis

The biosensor’s performance relies on the coupling of the core mode with the surface plasmon polariton mode. In this design, the x-polarized mode is utilized to assess sensor efficiency. The objective of developing a biosensor for cancer diagnosis is to examine the differences in refractive indices between normal and cancer cells. This study analyzed six types of cancer cells, including cervical, skin, blood, adrenal gland (A-G), and two types of breast cancer. Table 1 lists the refractive indices for normal and cancer cells across these six types of cancer.

Figure 4 shows the dispersion and CL for the x and y-polarized modes, along with the surface plasmon polariton mode of the biosensor, with the refractive index set at $n_a = 1.368$. The parameters are fixed at $P = 3.5\text{ }\mu\text{m}$, $r = 2.7\text{ }\mu\text{m}$, $d_1 = 1.8\text{ }\mu\text{m}$, $d_2 = 3.2\text{ }\mu\text{m}$, $d_3 = 1.3\text{ }\mu\text{m}$, $t_{\text{au}} = 40\text{ nm}$, and $t_t = 10\text{ nm}$. The yellow color indicates the losses associated with the y-polarized mode, which will not be discussed further due to its low peak value. The green curve represents the CL of the fundamental x-polarized mode, ranging from 600 to 750 nm. In contrast, the red and black curves illustrate the real part of the effective refractive index for the x-polarized mode and the surface plasmon polariton mode, respectively. The CL of the green curve peaks at 649 nm, where the effective refractive index of this mode aligns with the real part of the SPP mode. This wavelength is known as the resonant

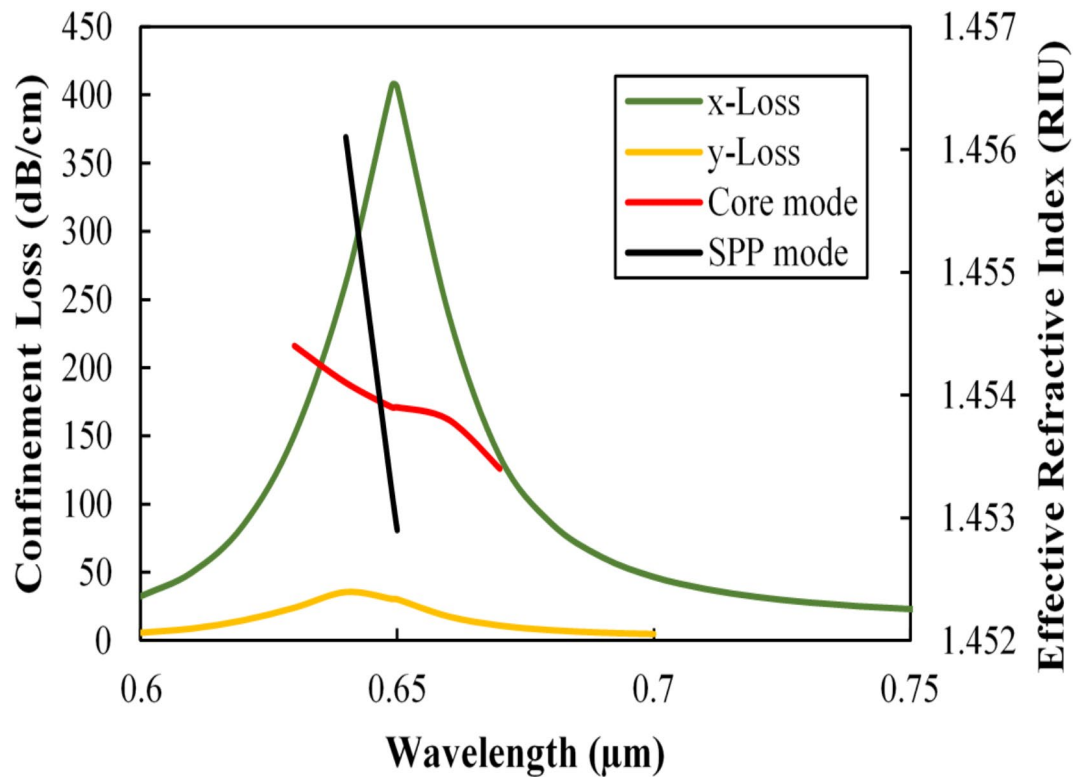


Fig. 4. Dispersion of fundamental mode (red line), SPP mode (black line), the loss spectrum of x-mode (green line), and y-mode (yellow line) that the parameters are fixed in $n_a = 1.368$, $d_1 = 1.8 \mu\text{m}$, $d_2 = 3.2 \mu\text{m}$, $d_3 = 1.3 \mu\text{m}$, $r = 2.7 \mu\text{m}$, $P = 3.5 \mu\text{m}$, $t_{\text{au}} = 40 \text{ nm}$, and $t_i = 10 \text{ nm}$.

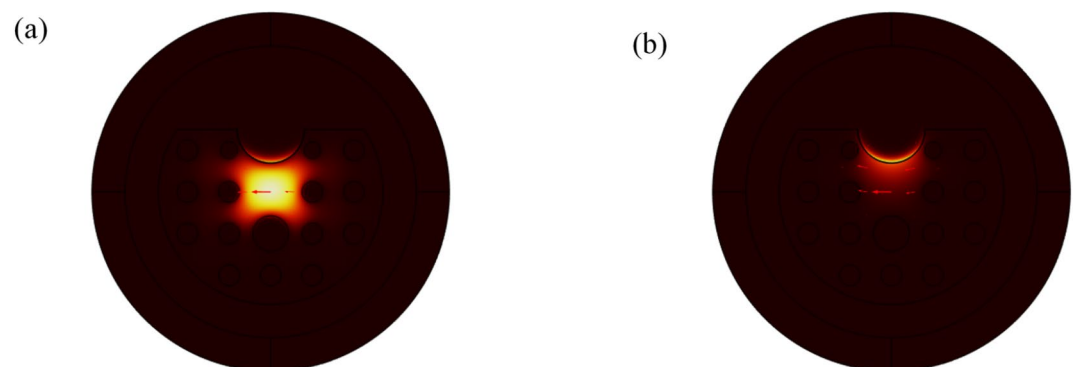


Fig. 5. The field distribution of **a** fundamental x-polarization mode and **b** the SPP mode.

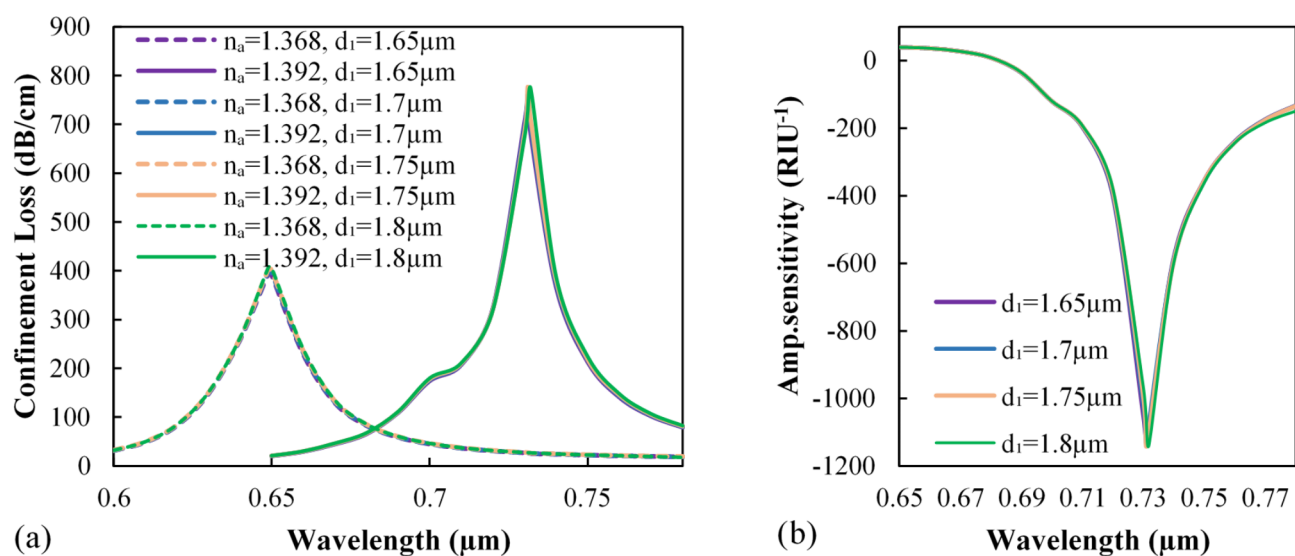
wavelength, indicating the phase-matching point of the effective refractive index. The interaction between the fundamental mode and the surface plasmon polariton mode significantly impacts sensor performance. Figure 5 shows the electric field distribution of both modes at the resonant wavelength. The electric field is concentrated near the channel and core, indicating the coupling between the core and SPP mode.

Changes in the sensor's structural parameters significantly affect its performance. We explored seven key parameters, detailed in Table 2 and shown in Figs. 6, 7, 8, 9, 10, 11 and 12.

Effect of air hole radius on biosensor performance

The geometrical parameters are examined to enhance the sensor's sensitivity to detecting cervical cancer. Three different sizes of air hole radii (d) are simulated. The first analysis focuses on the cladding air hole (d_1), as shown in Fig. 6. The refractive indices of healthy and cancer cells in the experiment are 1.368 and 1.392, respectively. Table 2 indicates that changing d_1 has minimal impact on the resonance wavelength in this cancer type, as the x-polarized mode is strongly confined in the core region. The amplitude sensitivity ranges from -1121.1 RIU^{-1}

Parameter	λ_{peak} (nm)	λ_{peak} (nm)	CL (dB/cm)	CL (dB/cm)	AS (RIU ⁻¹)
	Healthy cell $n_a = 1.368$	Cancerous cell $n_a = 1.392$	Healthy cell $n_a = 1.368$	Cancerous cell $n_a = 1.392$	
d_1 (μm)					
1.65	649	731	394.2	745.4	− 1,121.1
1.70	649	731	398.7	761.1	− 1,131.5
1.75	649	731	403.0	776.9	− 1,142.0
1.80	649	732	407.2	771.8	− 1,134.4
d_2 (μm)					
3.1	649	731	385.8	747.5	− 1,141.4
3.2	649	731	403.0	776.9	− 1,142.0
3.3	649	732	421.0	727.7	− 1,038.1
3.4	649	732	440.0	747.4	− 1,026.0
d_3 (μm)					
1.2	649	732	402.9	724.6	− 1,069.6
1.3	649	731	403.0	776.9	− 1,142.0
1.4	649	731	402.9	753.1	− 1,111.7
P (μm)					
3.5	649	731	403.0	776.9	− 1,142.0
3.6	649	729	330.4	830.3	− 1,431.7
3.7	649	728	274.6	689.7	− 1,387.8
r (μm)					
2.7	649	729	330.4	830.3	− 1,431.7
2.75	649	733	343.7	849.8	− 1,481.1
2.8	650	733	357.3	805.7	− 1350.5
t_{au} (nm)					
35	635	715	533.8	558.8	− 781.91
40	649	733	343.7	849.8	− 1,481.1
45	660	743	230.6	447.7	− 926.9
t_i (nm)					
8	649	729	352.5	707.7	− 1,162.4
10	649	733	343.7	849.8	− 1,481.1
12	649	732	334.1	748.2	− 1,291.7

Table 2. Optimized parameters for detecting cervical cancer cells.**Fig. 6.** Changes of (a) confinement loss spectrum for varying d_1 and (b) amplitude sensitivity curves for varying d_1 with RI value between 1.368 and 1.392.

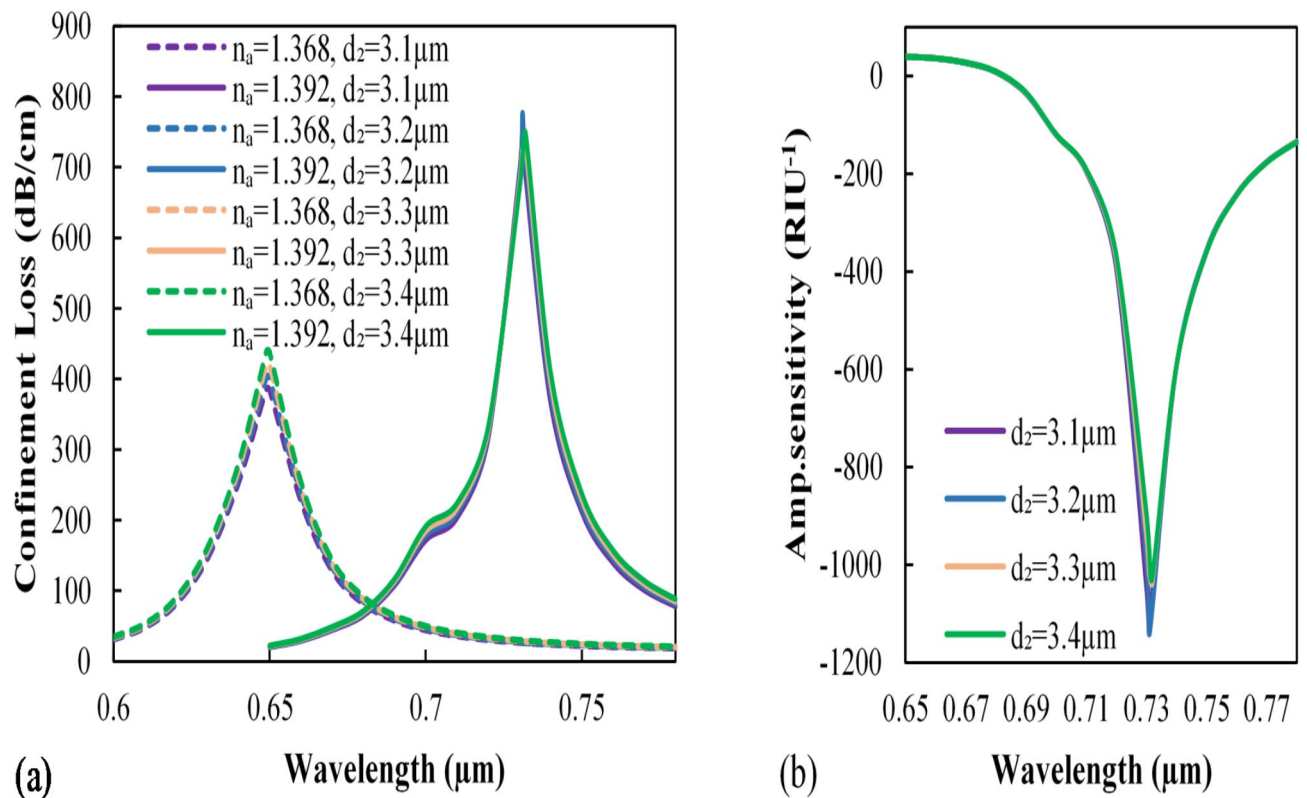


Fig. 7. Changes of (a) confinement loss for varying d_2 and (b) amplitude sensitivity values for varying d_2 with RI value between 1.368 and 1.392.

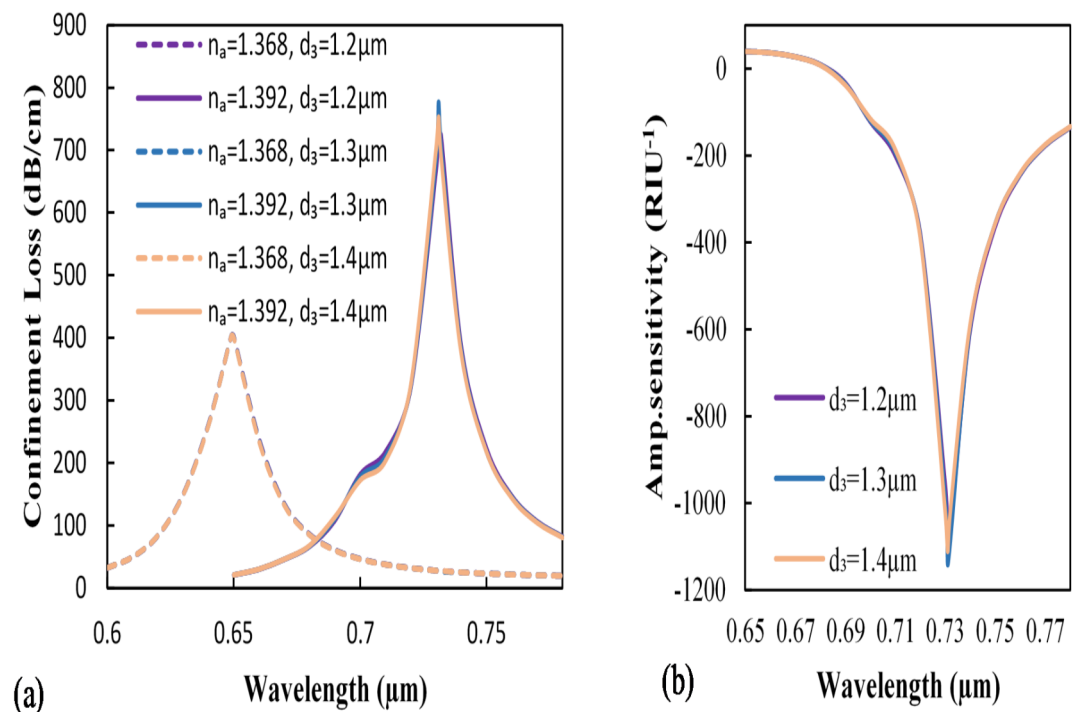


Fig. 8. Changes of a confinement loss for varying d_3 and b amplitude sensitivity curves for varying d_3 with RI value between 1.368 and 1.392.

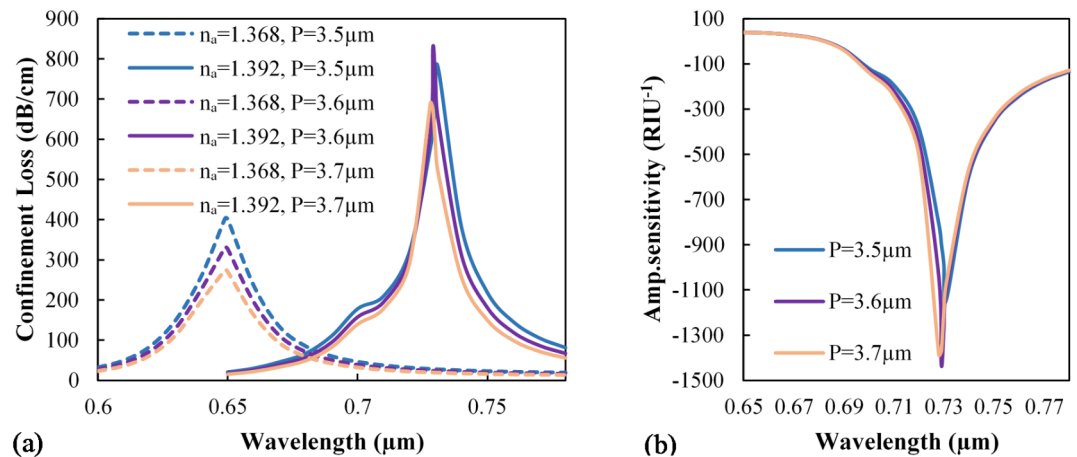


Fig. 9. Variations in **a** confinement loss and **b** amplitude sensitivity based on pitch adjustments with RI value between 1.368 and 1.392.

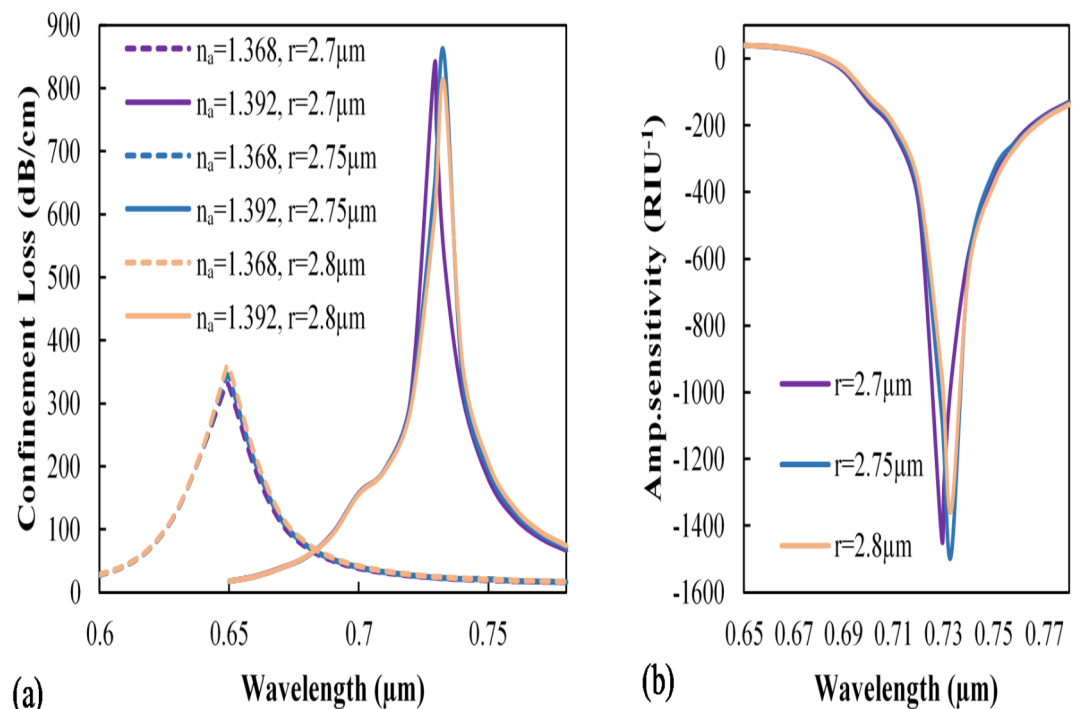


Fig. 10. Changes of **a** confinement loss for varying r and **b** amplitude sensitivity curves for varying r with RI value between 1.368 and 1.392.

to -1142 RIU^{-1} . Based on Fig. 6b; Table 2, the biosensor's amplitude sensitivity peaks at $d_1 = 1.75 \mu\text{m}$, which will be applied in subsequent studies.

The largest air hole is located at the bottom of the core. This hole, referred to as d_2 , enables energy transfer from the center of the structure to the microchannel. Figure 7a illustrates that the air hole comes in four sizes, ranging from $3.1 \mu\text{m}$ to $3.4 \mu\text{m}$, with steps of $0.1 \mu\text{m}$. Furthermore, Fig. 7b; Table 2 show that the AS ranges from -1026 RIU^{-1} to -1142 RIU^{-1} , with the highest sensitivity noted at $d_2 = 3.2 \mu\text{m}$.

The two holes adjacent to the microchannel, denoted as d_3 , are smaller than the previously mentioned holes. This size reduction facilitates the core's leakage into the plasmonic material. The effect of hole size ranging from $1.2 \mu\text{m}$ to $1.4 \mu\text{m}$, with an increment of $0.1 \mu\text{m}$, has been examined while keeping other parameters constant. Figure 8a shows how varying air hole sizes impact confinement loss. The amplitude sensitivity values, as indicated in Fig. 8b; Table 2, are $-1,069.6 \text{ RIU}^{-1}$, $-1,142 \text{ RIU}^{-1}$, and $-1,111.7 \text{ RIU}^{-1}$. For this study, d_3 is set at $1.3 \mu\text{m}$.

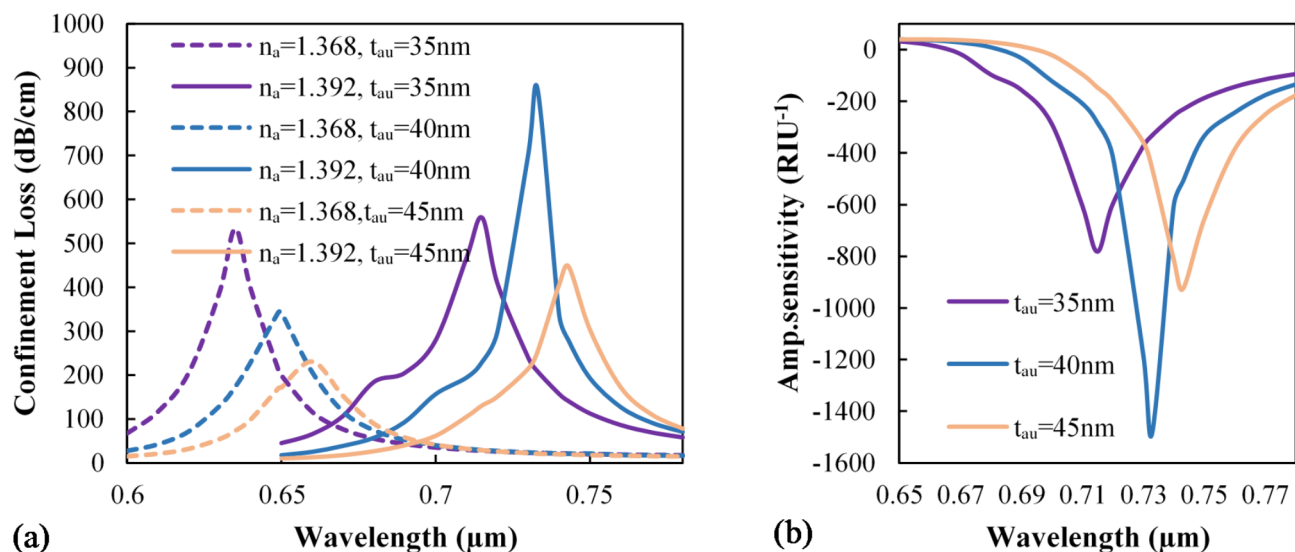


Fig. 11. Variation of (a) curve of confinement loss and (b) amplitude sensitivity with RI of $n_a = 1.368$ and 1.392 for different values of Au thicknesses.

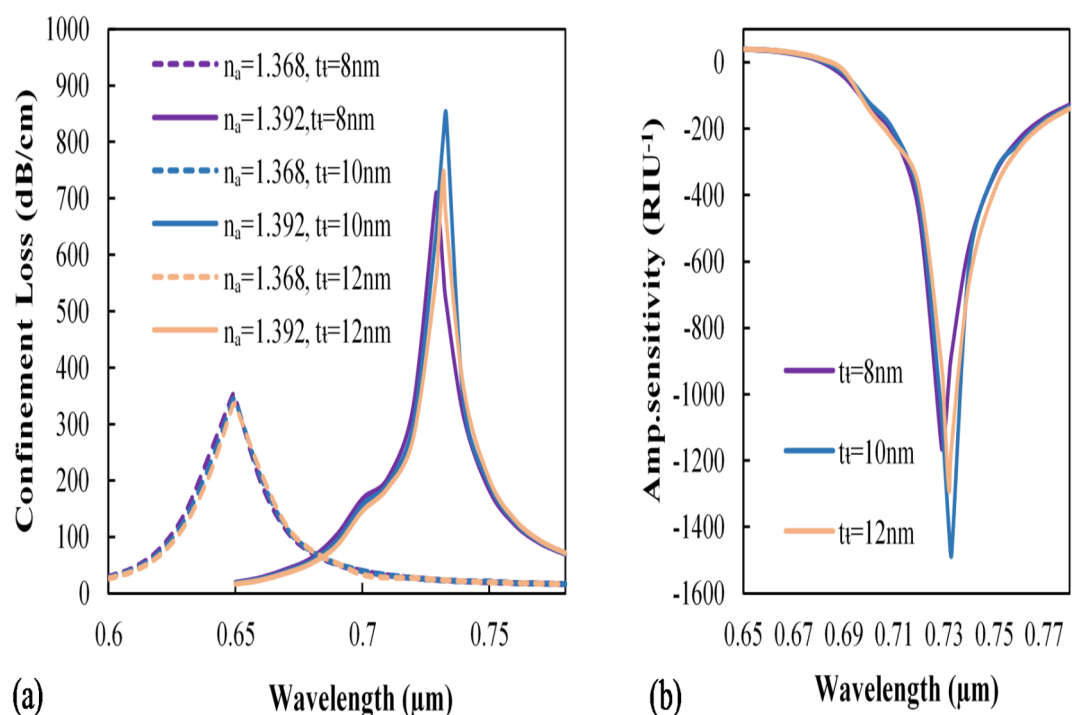


Fig. 12. Variation of (a) curve of confinement loss and (b) amplitude sensitivity with RI of $n_a = 1.368$ and 1.392 for different values of TiO₂ thicknesses.

Impact of pitch and open-channel on biosensor performance

The effect of pitch size is analyzed in Fig. 9, illustrating the loss spectra and amplitude sensitivity. As the parameter P increases from $3.5\text{ }\mu\text{m}$ to $3.6\text{ }\mu\text{m}$, the resonance peak at $n_a = 1.392$ shows a slight blueshift, changing the wavelength from 731 nm to 729 nm . Additionally, the amplitude sensitivity changes from -1142 RIU^{-1} to -1431.7 RIU^{-1} , as illustrated in Fig. 9b. This change is caused by the confinement of light in the central area. Figure 9a; Table 2 illustrate that variations in hole pitch have a minimal effect on the resonance wavelength, and the highest amplitude sensitivity is observed at $P = 3.6\text{ }\mu\text{m}$, which will be used in further studies.

Figure 10a demonstrates the impact of changing the open-channel radius. The microchannel diameter increases from $2.7\text{ }\mu\text{m}$ to $2.8\text{ }\mu\text{m}$ in $0.05\text{ }\mu\text{m}$ increments. At $r = 2.75\text{ }\mu\text{m}$, the confined loss in the HeLa cell rises significantly from 343.7 dB/cm to 849.8 dB/cm . According to Fig. 10b, amplitude sensitivity varies slightly

with changes in the value of r . Specifically, the amplitude sensitivity values at 2.7, 2.75, and 2.8 μm are -1431.7 , -1481.1 , and -1350.5 RIU^{-1} , respectively.

Impact of plasmonic material thickness on the performance

The plasmonic material is essential for surface plasmon excitation, as it couples the core and surface plasmon modes. This necessitates an investigation into the effects of the thicknesses of the Au and TiO_2 layers. As shown in Table 2; Fig. 11a, t_{Au} increases from 35 nm to 45 nm in the context of cervical cancer, with the following parameters held constant: $d_1 = 1.75 \mu\text{m}$, $d_2 = 3.2 \mu\text{m}$, $d_3 = 1.3 \mu\text{m}$, $P = 3.6 \mu\text{m}$, $r = 2.75 \mu\text{m}$, and $t_t = 10 \text{ nm}$. Additionally, the peak of the CL experiences a redshift, moving from wavelengths of 635, 649, and 660 nm to 715, 733, and 743 nm. The biosensor experiences a maximum CL of about 849.8 dB/cm at t_{Au} of 40 nm with refractive indices of 1.392, leading to a peak amplitude sensitivity of -1481.1 RIU^{-1} . Selecting the appropriate thickness of these materials is crucial, as it impacts the decay rate of both SPR and evanescent waves. Additionally, increasing the thickness beyond 40 nm can complicate the fabrication process⁴⁶.

The confinement loss of titanium dioxide as a function of wavelength is illustrated in Fig. 12a. The investigated thicknesses were 8 nm, 10 nm, and 12 nm. At 10 nm, the titanium dioxide coating exhibited a confinement loss of 849.8 dB/cm for a refractive index of 1.392 at $\lambda = 733 \text{ nm}$, which was higher than at 8 nm. Figure 12b shows the amplitude sensitivity curves with values of $-1,162.4$, $-1,481.1$, and $-1,291.7 \text{ RIU}^{-1}$ for thicknesses of 8, 10, and 12 nm, respectively.

Detection of cancer cells

Using the refractive indices in Table 1 and the suggested biosensor, the visuals in this section demonstrate the optical characteristics at various wavelengths for healthy and diseased biological samples across six types of cancer cells. Figure 13a–f depict the confinement loss of the open D-channel PCF-SPR biosensor, emphasizing key performance outcomes in the detection of Basal, HeLa, Jurkat, and PC12 cells, as well as two types of breast cancer (MDA-MB-231 and MCF-7).

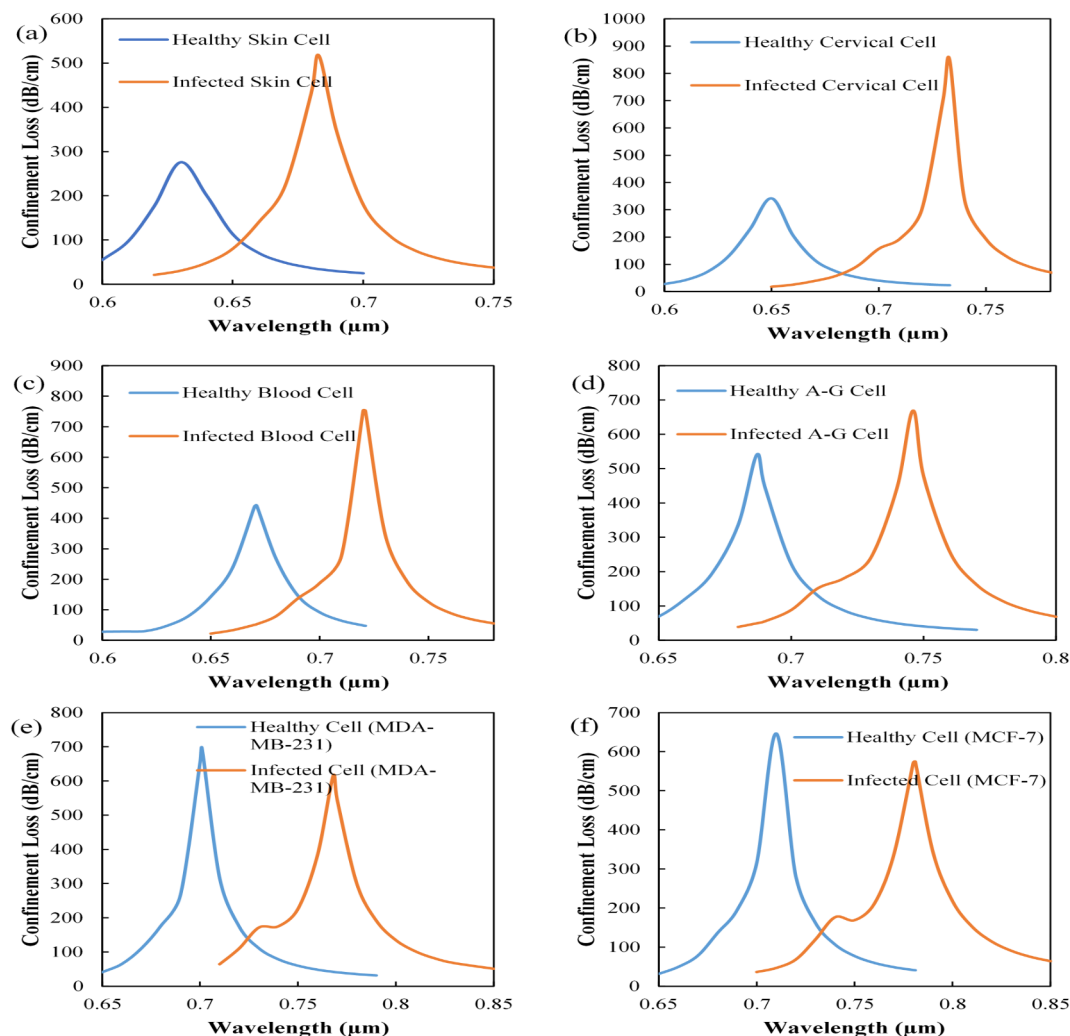


Fig. 13. Results related to the detection of skin, cervical, blood, adrenal gland, and two types of breast cancer (MDA-MB-231 and MCF-7) using the proposed biosensor.

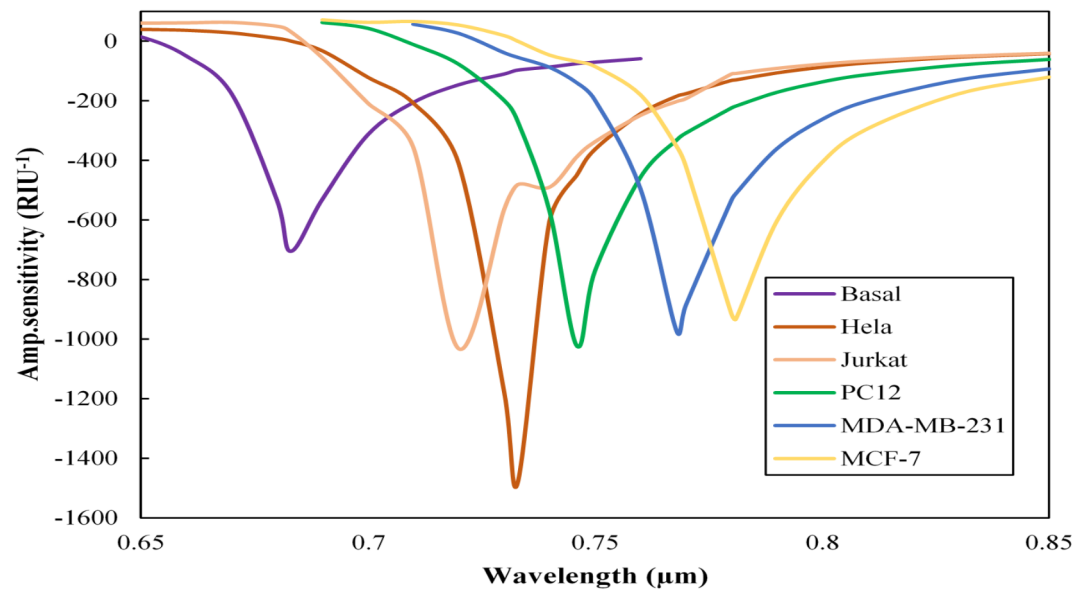


Fig. 14. Amplitude sensitivity for six types of cancer cells: Basal, HeLa, Jurkat, PC12, MDA-MB-231, and MCF-7.

Cancer type	Cell type	WS (nm/RIU)	AS (RIU ⁻¹)	FWHM (nm)	FOM (RIU ⁻¹)	Resolution (RIU)	SNR	DL
Skin	Basal	2,600.00	− 705.49	20	130	1.92 × 10 ⁻⁵	2.60	10.50
Cervical	HeLa	3,500.00	− 1,481.09	10	350	1.19 × 10 ⁻⁵	8.40	3.92
Blood	Jurkat	3,571.42	− 1,057.73	15	238.09	2.00 × 10 ⁻⁵	3.33	7.40
Adrenal gland	PC12	4,214.28	− 1,022.64	20	210.71	1.69 × 10 ⁻⁵	2.95	10.17
Breast	MDA-MB-231	4,785.71	− 974.16	25	191.42	1.49 × 10 ⁻⁵	2.68	13.03
Breast	MCF-7	5,214.28	− 933.23	30	173.80	1.37 × 10 ⁻⁵	2.43	16.01

Table 3. Evaluation of the Sensor’s performance at optimal design parameters for identifying various cancer cell types.

According to Fig. 13, altering the refractive index of a healthy cell and transforming it into a cancerous cell impacts the coupling of the incident light wave to the surface plasmon wave. This change leads to the detection and identification of cancer and a shift in the resonance wavelength, resulting in a redshift. One of the most common methods for evaluating sensor performance is through spectral sensitivity. This concept can be explained using Eq. (12), which analyzes the changes in wavelengths related to the loss peak and variations in the refractive index. Furthermore, sensor performance can be assessed through the amplitude sensitivity at a specific wavelength, which is determined using Eq. (13). While wavelength sensitivity, or wavelength interrogation techniques, requires spectral manipulation and can be costly and complex to implement, amplitude interrogation is more commonly used due to its cost-effectiveness and simpler application. Spectral and amplitude sensitivity values were obtained from various cancer cell types, including 2,600, 3,500, 3,571.42, 4,214.28, 4,785.71, and 5,214.28 nm/RIU, as well as − 705.49, − 1,481.09, − 1,057.73, − 1,022.64, − 974.16, and − 933.23 RIU⁻¹ for Basal, HeLa, Jurkat, PC12, MDA-MB-231, and MCF-7 cells. According to Fig. 14; Table 3, which compare the performance of the six cell types, the sensor outperforms the other cells in amplitude sensitivity, FOM, resolution, and full width at half maximum with results of -1,481.09 RIU⁻¹, 350 RIU⁻¹, 1.19 × 10⁻⁵ RIU, and 10 nm. Also, there is an inverse relationship between SNR and FWHM, as described in Eq. (16); an optimal SNR is achieved when FWHM is minimized. As a result, the highest recorded SNR value was 7 for HeLa cells. The proposed biosensor has a minimum detection limit of 3.92 and a maximum of 16.01. The proposed D-channel biosensor demonstrates exceptional sensitivity, FOM, resolution, SNR, and DL, indicating that this sensor provides high sensing performance and is easily manufactured.

Figure 15 illustrates the polynomial fit of the refractive index for normal and cancer cells, which varies from 1.36 to 1.401. The graph demonstrates that as the refractive index increases, resonance occurs at longer wavelengths. The sensor’s linear response is evaluated using the R-squared (R²) value, with a higher R² indicating a better linear correlation. In our proposed biosensor, the R² value is calculated to be 0.9997, suggesting that the biosensor demonstrates a strong and consistent response in the early detection of cancer.

Table 4 highlights the similarities between previous SPR-based cancer detection studies and our design, indicating that our sensor offers notable advantages in resolution, spectral, and amplitude sensitivity.

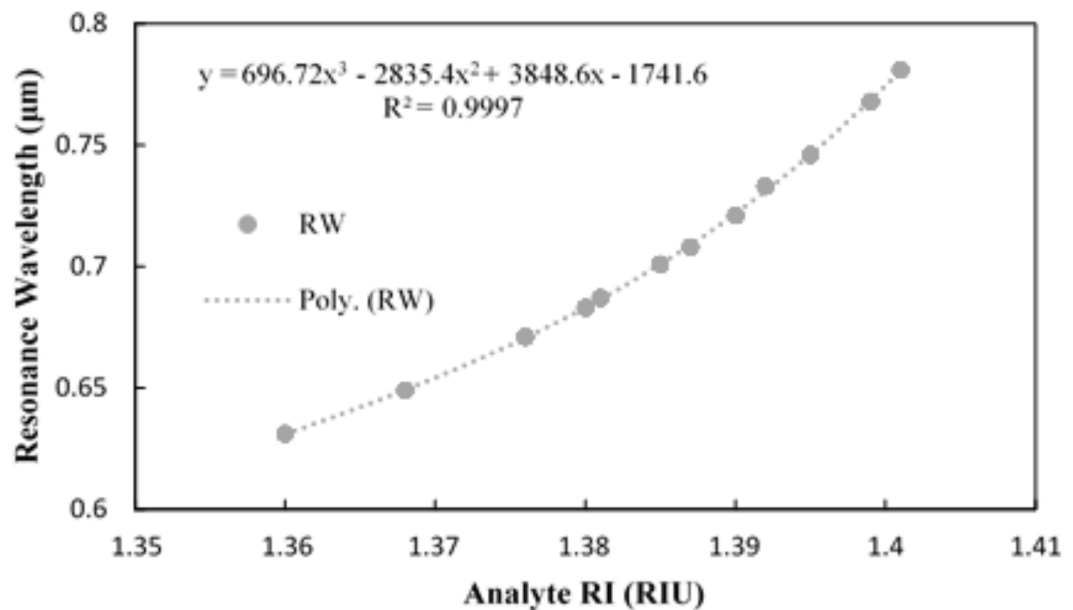


Fig. 15. Fitting polynomials to the resonance wavelengths in response to changes in refractive index for both normal and cancerous cells.

Furthermore, its straightforward structure and exceptional sensing performance allow it to detect analytes across a wide concentration range. In conclusion, this biosensor is an excellent option for detecting various molecules.

It is crucial to understand that the simulation was based on the assumption of stable environmental conditions. The detection of the sample relies on changes in its refractive index. Achieving consistent sensitivity and specificity across different cancer cell types is challenging due to the variable SPR responses from different environments. Factors such as temperature fluctuations and sample impurities can affect sensor accuracy. Additionally, practical challenges like integrating the technology into clinical workflows, scaling for mass production, and maintaining cost-efficiency must be addressed for effective real-world implementation⁴⁷.

Furthermore, the experimental results obtained after fabrication may be influenced by noise. Three main types of noise can impact sensor performance: shot noise, fluctuations in the intensity of the light source, and variations in the conversion efficiency of the detector. These factors can be analyzed using various available techniques^{48,49}.

Conclusion

SPR and Photonic Crystal are both advanced technologies with unique properties that can be harnessed for biosensing applications, including early cancer detection. In our proposed open D-channel PCF-SPR biosensor, we utilize gold due to its favorable properties for surface plasmon resonance and ease of fabrication, which ultimately reduces manufacturing complexity. It also includes a thin layer of TiO_2 to improve the adhesion of Au and silica. The design incorporates a square lattice with holes of three different sizes to improve the biosensor's performance. This variation allows better light interaction with biochemical samples, maximizing resonance shifts when target biomolecules bind. Numerical simulations of the PCF-based SPR biosensor were performed using the FEM. This biosensor shows the highest response for six cancer cells. We utilize spectral and amplitude interrogation techniques to identify small changes in the refractive index of cells associated with six types of cancer. HeLa cells exhibit the highest amplitude sensitivity, resolution, and figure of merit, with values of $-1,481.09 \text{ RIU}^{-1}$, $1.19 \times 10^{-5} \text{ RIU}$, and 350 RIU^{-1} . Additionally, MCF-7 cells have the highest wavelength sensitivity, recorded at $5,214.28 \text{ nm/RIU}$. These values demonstrate the sensor's capability to detect minute changes, which is crucial for early cancer detection. Additionally, the sensor proposed demonstrates a maximum spectral sensitivity of $47,000 \text{ nm/RIU}$ within the refractive index range of 1.25 to 1.43. This high-tolerance biosensor can be manufactured easily using existing photonic crystal fiber fabrication technologies. It has numerous applications in medicine and biological analysis, which can be used to detect proteins, viruses, RNA/DNA strands, and various chemical compounds that fall within the specified refractive index range.

Biosensor type	Cell type	Spectral sensitivity (nm/RIU)	Amp. sensitivity (RIU ⁻¹)	Resolution (RIU)	References
C-grooved PCF-SPR	Basal	1,500.00	− 447.97	6.70×10^{-5}	28
	HeLa	1,666.67	− 1058.03	6.00×10^{-5}	
	Jurkat	1,428.57	− 396.29	7.00×10^{-5}	
	PC12	1,428.57	− 489.66	7.00×10^{-5}	
	MDA-MB-231	2,142.86	− 824.96	4.67×10^{-5}	
	MCF-7	2,142.86	− 721.55	4.67×10^{-5}	
Dual-Core PCF-SPR	Basal	3,000.0	− 307.281	3.33×10^{-5}	30
	HeLa	4,166.7	− 555.229	2.40×10^{-5}	
	Jurkat	4,285.7	− 440.405	2.33×10^{-5}	
	PC12	5,000.0	− 575.345	2.00×10^{-5}	
	MDA-MB-231	5,714.3	− 711.482	1.75×10^{-5}	
	MCF-7	6,428.6	− 766.361	1.55×10^{-5}	
PCF-SPR	Basal	3,150.00	− 625	3.2×10^{-5}	50
	HeLa	4,333.33	− 757	2.3×10^{-5}	
	Jurkat	4,642.86	− 401	2.2×10^{-5}	
	PC12	5,500.00	− 399	1.8×10^{-5}	
	MDA-MB-231	6,428.57	− 324	1.6×10^{-5}	
	MCF-7	7,142.86	− 305	1.4×10^{-5}	
H-shaped PCF-SPR	Basal	4,000.00	− 422.7596	2.50×10^{-5}	51
	HeLa	5,000.00	− 792.8853	1.27×10^{-5}	
	MDA-MB-231	7,857.14	− 985.2674	2.00×10^{-5}	
Open D-channel PCF-SPR	Basal	2,600.00	− 705.49	1.92×10^{-5}	Proposed work
	HeLa	3,500.00	− 1,481.09	1.19×10^{-5}	
	Jurkat	3,571.42	− 1,057.73	2.00×10^{-5}	
	PC12	4,214.28	− 1,022.64	1.69×10^{-5}	
	MDA-MB-231	4,785.71	− 974.16	1.49×10^{-5}	

Table 4. Comparative analysis of the most recent biosensors for the detection of cancer.

Data availability

The datasets used and analyzed during the current study are available from the corresponding author upon reasonable request.

Received: 24 December 2024; Accepted: 19 March 2025

Published online: 24 March 2025

References

- Triveni, C., Krupa, V., Bahaddur, I. & Yashaswini, P. Photonic crystal-based biosensor to detect multiple myeloma from blood serum. *J. Opt.* **53**, 383–388 (2024).
- Arya, L. et al. Investigation of machine learning algorithms and plasmonic Waveguide-Based Fano resonance sensor for diagnosis of Estrogen. *Plasmonics*, 1–11 (2024).
- Seyfried, T. N. & Shelton, L. M. Cancer as a metabolic disease. *Nutr. Metabolism*. **7**, 1–22 (2010).
- Gowdhami, D., Balaji, V., Murugan, M., Robinson, S. & Hegde, G. Photonic crystal based biosensors: an overview. *ISSS J. Micro Smart Syst.* **11**, 147–167 (2022).
- Scullion, M. G., Krauss, T. F. & Di Falco, A. Slotted photonic crystal sensors. *Sensors* **13**, 3675–3710 (2013).
- Kumar, S. & Singh, R. Recent optical sensing technologies for the detection of various biomolecules. *Opt. Laser Technol.* **134**, 106620 (2021).
- Wang, W. et al. A label-free fiber optic SPR biosensor for specific detection of C-reactive protein. *Sci. Rep.* **7**, 16904 (2017).
- Sharma, S. & Mishra, S. K. Exploiting the advantages of Ag/ITO/Enzyme trapped gel layers to develop a highly sensitive and selective fiber optic plasmonic Urea sensor. *Chemosensors* **11**, 421 (2023).
- Singh, S. et al. A review on various sensing prospects of SPR based photonic crystal fibers. *Photonics Nanostructures-Fundamentals Appl.* **54**, 101119 (2023).
- Chaudhary, V. S., Kumar, D. & Kumar, S. Gold-immobilized photonic crystal fiber-based SPR biosensor for detection of malaria disease in human body. *IEEE Sens. J.* **21**, 17800–17807 (2021).
- Danlard, I. & Akowuah, E. K. Assaying with PCF-based SPR refractive index biosensors: from recent configurations to outstanding detection limits. *Opt. Fiber. Technol.* **54**, 102083 (2020).
- Nijhum, J. M. & Ahmed, T. Highly sensitive quasi-D-shaped photonic crystal fiber biosensor designed for the detection of RBC parasitized by Plasmodium falciparum for the early diagnosis of malaria. *Optics Continuum*. **2**, 1315–1330 (2023).
- Sharma, M., Mishra, S. K. & Ung B. Ultra-sensitive and large dynamic range refractive index sensor utilizing annular core photonic crystal fiber. In *Photonic fiber and crystal devices: advances in materials and innovations in device applications XIII*. 13–19 (SPIE).
- Azad, S., Khosravi, M., Nikzad, A. & Mishra, S. K. A novel contemporary molecular imprinting technique for non-enzymatic selective glucose detection. *Opt. Laser Technol.* **148**, 107786 (2022).
- Singh, L. et al. Assessment of refractive index-based SPR sensor for branched chain AA. *Plasmonics* **19**, 2391–2400 (2024).
- Azab, M., Hameed, M. & Obayya, S. Overview of optical biosensors for early cancer detection: fundamentals, applications and future perspectives. *Biology*, **12** (2), 232 (2023).

17. Gonzalez-Gonzalez, E. et al. Colorimetric loop-mediated isothermal amplification (LAMP) for cost-effective and quantitative detection of SARS-CoV-2: the change in color in LAMP-based assays quantitatively correlates with viral copy number. *Anal. Methods*. **13**, 169–178 (2021).
18. Chopra, R., Wagner, S. K. & Keane, P. A. Optical coherence tomography in the 2020s—outside the eye clinic. *Eye* **35**, 236–243 (2021).
19. Kumar, D., Khurana, M., Sharma, M. & Singh, V. Analogy of gold, silver, copper, and aluminum-based ultra-sensitive surface plasmon resonance photonic crystal fiber biosensors. *Mater. Today Proc.* (2023).
20. Kaur, V. & Singh, S. A dual-channel surface plasmon resonance biosensor based on a photonic crystal fiber for multianalyte sensing. *J. Comput. Electron.* **18**, 319–328 (2019).
21. Anik, M. H. K. et al. Milled microchannel-assisted open D-channel photonic crystal fiber plasmonic biosensor. *IEEE Access*. **9**, 2924–2933 (2020).
22. Yang, X., Hou, S., Xie, C., Wu, G. & Yan, Z. High-performance photonic crystal fiber biosensor based on surface plasmon resonance for early cancer detection. *Plasmonics* **19**, 675–685 (2024).
23. Abdelghaffar, M. et al. Highly sensitive V-shaped SPR PCF biosensor for cancer detection. *Opt. Quant. Electron.* **55**, 472 (2023).
24. Ibrahim, K. M., Kumar, R. & Pakhira, W. Enhance the design and performance analysis of a highly sensitive twin-core PCF SPR biosensor with gold plating for the early detection of cancer cells. *Plasmonics* **18**, 995–1006 (2023).
25. Teng, C., Wang, Y. & Yuan, L. Polymer optical fibers based surface plasmon resonance sensors and their applications: A review. *Opt. Fiber. Technol.* **77**, 103256 (2023).
26. Mishra, A. K., Mishra, S. K. & Singh, A. P. Giant infrared sensitivity of surface plasmon resonance-based refractive index sensor. *Plasmonics* **13**, 1183–1190 (2018).
27. Liu, Q., Li, S., Chen, H., Li, J. & Fan, Z. High-sensitivity plasmonic temperature sensor based on photonic crystal fiber coated with nanoscale gold film. *Appl. Phys. Express*. **8**, 046701 (2015).
28. Ibrahim, K. M., Kumar, R. & Pakhira, W. C-grooved dual-core PCF SPR biosensor with Graphene/au coating for enhanced early cancer cell detection. *Appl. Phys. A*. **130**, 439 (2024).
29. Mumtaz, F. et al. MXene (Ti₃C₂Tx) coated highly-sensitive D-shaped photonic crystal fiber-based SPR biosensor. *Photonics Nanostructures-Fundamentals Appl.* **52**, 101090 (2022).
30. Arafat, S., Fatema, T. & Rahman, M. S. Numerical analysis and detection of cancer cells using a dual-core gold coated plasmonic biosensor. *Opt. Mater. Express*. **14**, 1603–1619 (2024).
31. Sazio, P. J. et al. Microstructured optical fibers as high-pressure microfluidic reactors. *Science* **311**, 1583–1586 (2006).
32. An, G., Hao, X., Li, S., Yan, X. & Zhang, X. D-shaped photonic crystal fiber refractive index sensor based on surface plasmon resonance. *Appl. Opt.* **56**, 6988–6992 (2017).
33. Maier, S. (Springer, (2007).
34. Tien, C. L., Lin, H. Y. & Su, S. H. High Sensitivity Refractive Index Sensor by D-Shaped Fibers and Titanium Dioxide Nanofilm. *Adv. Condens. Matter Phys.* 2303740 (2018).
35. DeVore, J. R. Refractive indices of rutile and sphalerite. *JOSA* **41**, 416–419 (1951).
36. Jahan, N. et al. Photonic crystal fiber based biosensor for Pseudomonas bacteria detection: A simulation study. *IEEE Access*. **9**, 42206–42215 (2021).
37. Fakhri, M. A. et al. Investigations on device structure and sensing mechanism using gold nanoparticles decorated photonic crystal fiber-based biosensors. *Plasmonics* **19**, 533–550 (2024).
38. Gandhi, M. A., Senthilnathan, K., Babu, P. R. & Li, Q. Visible to near-infrared highly sensitive micro biosensor based on surface plasmon polariton with external sensing approach. *Results Phys.* **15**, 102590 (2019).
39. Pysz, D. et al. Stack and draw fabrication of soft glass microstructured fiber optics. *Bull. Pol. Acad. Sci. Tech. Sci.* **62**, 667–682 (2014).
40. van Brakel, A., Grivas, C., Petrovich, M. N. & Richardson, D. J. Micro-channels machined in microstructured optical fibers by femtosecond laser. *Opt. Express*. **15**, 8731–8736 (2007).
41. Martelli, C. et al. Micromachining structured optical fibers using focused ion beam milling. *Opt. Lett.* **32**, 1575–1577 (2007).
42. Cordeiro, C. M. et al. Towards practical liquid and gas sensing with photonic crystal fibers: side access to the fiber microstructure and single-mode liquid-core fiber. *Meas. Sci. Technol.* **18**, 3075 (2007).
43. Singh, L. et al. Investigation of SPR sensor for Immunoglobulin detection by using Ag–Si₃N₄–BP on the sensing layer. *Opt. Quant. Electron.* **56**, 771 (2024).
44. Cremers, V., Puurunen, R. L. & Dendooven, J. Conformality in atomic layer deposition: current status overview of analysis and modeling. *Appl. Phys. Reviews* **6** (2019).
45. Dutta, T. et al. Recent advances in Metal-Organic Framework-Based fiber optic sensors and photodetectors: synthesis, properties, and applications. *Chem. Eng. J.*, 160543 (2025).
46. Heinrich, S. et al. Comparison of ZrN and TiN formed by plasma-based ion implantation & deposition. *Surf. Coat. Technol.* **202**, 2310–2313 (2008).
47. Singh, S. et al. Gold immobilized SPR-Enhanced PCF biosensor for detection of cancer cells: a numerical simulation. *Plasmonics*, 1–10 (2024).
48. Dash, J. N., Das, R. & Jha, R. AZO coated microchannel incorporated PCF-based SPR sensor: a numerical analysis. *IEEE Photonics Technol. Lett.* **30**, 1032–1035 (2018).
49. Nenninger, G. G., Piliarik, M. & Homola, J. Data analysis for optical sensors based on spectroscopy of surface plasmons. *Meas. Sci. Technol.* **13**, 2038 (2002).
50. Yasli, A. Cancer detection with surface plasmon resonance-based photonic crystal fiber biosensor. *Plasmonics* **16**, 1605–1612 (2021).
51. Pappu, M. H., Rahman, A. & Mollah, M. A. An h-shaped exposed core surface plasmon resonance sensor and detection of cancer cells. *Plasmonics*, 1–17 (2024).

Acknowledgements

This research has been done in the Nano-photonics and Optoelectronics Research Laboratory (NORLab), Shahid Rajae Teacher Training University.

Author contributions

M. A.: designed and performed simulations, analyzed data, and wrote the manuscript, S. O.: contributed data, supervised, edited, and prepared the final draft of the manuscript, M. S.: reviewed and edited.

Funding

This work was supported by the Shahid Rajae Teacher Training University under grant number 5973.84.

Declarations

Competing interests

The authors declare no competing interests.

Additional information

Correspondence and requests for materials should be addressed to S.O.

Reprints and permissions information is available at www.nature.com/reprints.

Publisher's note Springer Nature remains neutral with regard to jurisdictional claims in published maps and institutional affiliations.

Open Access This article is licensed under a Creative Commons Attribution-NonCommercial-NoDerivatives 4.0 International License, which permits any non-commercial use, sharing, distribution and reproduction in any medium or format, as long as you give appropriate credit to the original author(s) and the source, provide a link to the Creative Commons licence, and indicate if you modified the licensed material. You do not have permission under this licence to share adapted material derived from this article or parts of it. The images or other third party material in this article are included in the article's Creative Commons licence, unless indicated otherwise in a credit line to the material. If material is not included in the article's Creative Commons licence and your intended use is not permitted by statutory regulation or exceeds the permitted use, you will need to obtain permission directly from the copyright holder. To view a copy of this licence, visit <http://creativecommons.org/licenses/by-nc-nd/4.0/>.

© The Author(s) 2025